REGIME-AWARE SEMI-SUPERVISED REGRESSION VIA CLUSTERING-GATED EXPERTS

Anonymous authors

Paper under double-blind review

ABSTRACT

We study regime-aware semi-supervised regression for tunnel boring machine (TBM) operation modeling under cross-strata nonstationarity and label scarcity. We propose CGE—Clustering-Gated Experts—a three-stage framework that (i) discovers latent geological regimes via robust, ensemble clustering; (ii) trains per-regime heterogeneous ensembles with agreement-based pseudo-labeling and consistency regularization; and (iii) routes predictions by a lightweight distance-based soft gate. For risk-aware deployment, we equip all predictors with conformalized quantile regression (CQR) to yield calibrated prediction intervals. On real TBM data with 5–20% label budgets, CGE surpasses strong semi-supervised baselines, achieving at 10% labels an average R^2 of 0.942 ± 0.018 and RMSE of 0.112 ± 0.015 . With 90% CQR intervals, it attains near-nominal coverage and the narrowest widths, alongside lower NLL/CRPS. Overall, CGE offers a practical accuracy—uncertainty trade-off for safety-critical TBM decision-making under nonstationary geology.

1 Introduction

In recent years, significant progress has been made in the prediction of shield tunneling parameters, with substantial advances in capturing the complex nonlinear dynamics during construction (Zhou et al., 2021; Sun et al., 2023; Chen et al., 2024). Shield tunneling data often exhibit highly nonstationary and time-varying patterns, such as cross-strata heterogeneity, multi-source feature coupling, and sensor noise interference. These characteristics impose considerable challenges for predictive modeling: on the one hand, models must possess the ability to characterize intricate patterns; on the other hand, they must avoid overfitting caused by limited data size and scarce labeled samples Rahim et al. (2024); Li et al. (2023).

When labeled data are limited, semi-supervised learning provides an important avenue for performance enhancement. Chen et al. (2021) proposed a semi-supervised support vector regression method that leverages unlabeled samples to improve generalization with few labeled instances. More recently, Jo et al. (2024) incorporated pseudo-label filtering and uncertainty estimation mechanisms, effectively reducing the negative impact of erroneous pseudo-labels on model training. These studies indicate that effectively exploiting unlabeled data is crucial to improving model stability under complex working conditions.

Meanwhile, the Mixture of Experts (MoE) paradigm has gained increasing attention in machine learning and artificial intelligence. The core idea is to use a gating mechanism to partition the input into different expert subnetworks, where each expert specializes in a particular scenario or data sub-distribution. The gating network then aggregates the outputs of all experts through weighted combinations. This mechanism has achieved remarkable success in domains such as natural language processing and computer vision Shazeer et al. (2017b); Fedus et al. (2022). However, in civil and tunneling engineering, current research remains largely focused on traditional ensemble methods or single-model optimization (Li et al., 2024a; Abbasi et al., 2024), with little systematic exploration of expert selection mechanisms for cross-strata prediction and uncertainty modeling.

Motivated by these challenges, this paper proposes **CGE**, a regime-aware semi-supervised regression framework tailored to TBM operation modeling with scarce labels and cross-strata drift. In the preprocessing stage, outlier removal and feature selection are conducted, followed by the use of multi-clustering algorithms to identify geological scenarios. Within each scenario, semi-supervised

regression models with heterogeneous ensembles are constructed to fully exploit the potential of unlabeled data. At the prediction stage, a clustering-based expert selection mechanism is employed for model routing, while uncertainty estimation provides predictive confidence to meet the safety requirements of high-risk tunneling operations.

The major contributions of this work are summarized as follows:

- 1. We propose a unified framework that integrates **geological scenario partitioning, semi-supervised regression, and expert selection**, capable of maintaining prediction accuracy and stability under cross-strata nonstationarity.
- We introduce pseudo-label filtering and uncertainty constraints in model training, effectively alleviating the performance bottleneck caused by insufficient labeled data.
- 3. We validate the proposed method on real-world shield tunneling datasets, demonstrating that it outperforms multiple baseline models while providing reliable uncertainty estimation alongside high-accuracy predictions.

2 RELATIVE WORK

2.1 ENSEMBLE LEARNING AND EXPERT MODELS

Ensemble learning, as an important means to enhance model robustness and generalization ability, has demonstrated superior performance across various prediction tasks. Expert models and Mixture-of-Experts (MoE) frameworks have become a recent research focus. The MoE framework allocates appropriate experts to inputs through gating functions, enabling adaptive prediction when data exhibit multiple scenarios and heterogeneous distributions (Kawata et al. (2025)).Rahman et al. (2024) proposed a gated ensemble spatiotemporal mixture-of-experts network (GESME-Net), which achieved remarkable performance in multi-task prediction. Wang et al. (2025) designed an MoE model with self-supervised aggregation for imbalanced regression tasks, effectively alleviating the challenge of uneven data scales across subtasks.

2.2 Semi-Supervised Learning and Uncertainty Quantification

In engineering contexts, it is common to encounter a scarcity of labeled samples while abundant unlabeled operational data remain underutilized. Semi-supervised learning (SSL) has therefore emerged as an effective approach to reduce labeling costs and enhance generalization ability. Recent methodological studies indicate that pseudo-labeling and consistency regularization constitute the two mainstream strategies: the former leverages high-confidence predictions as "soft/hard labels" for retraining, while the latter encourages consistency of model outputs under perturbations or data augmentations.

Fan et al. (2023) investigated consistency regularization strategies and found that simultaneously constraining both the feature space and the output space can substantially improve model stability under low-label conditions. Meanwhile, Kage & Bolívar (2024) summarized the evolution of pseudo-labeling from simple thresholding strategies to mechanisms incorporating confidence calibration and noise-robust correction, underscoring their applicability in scenarios with high annotation costs. In engineering applications(Xu et al. (2023)). applied generative or self-supervised strategies to geophysical and geological tasks for feature enhancement and low-label learning, significantly improving learning efficiency under complex media and non-stationary conditions.

3 Methodology

3.1 Overview

As shown in Figure 1, the model consists of three sequential stages: geological clustering, semisupervised learning, and expert integration. First, geological features and operational parameters are extracted to perform clustering and embedding, thereby constructing representative geological scenarios. Subsequently, within each scenario, sparse labeled samples are combined with unlabeled data, and a semi-supervised mechanism is employed for label expansion and quality control, which

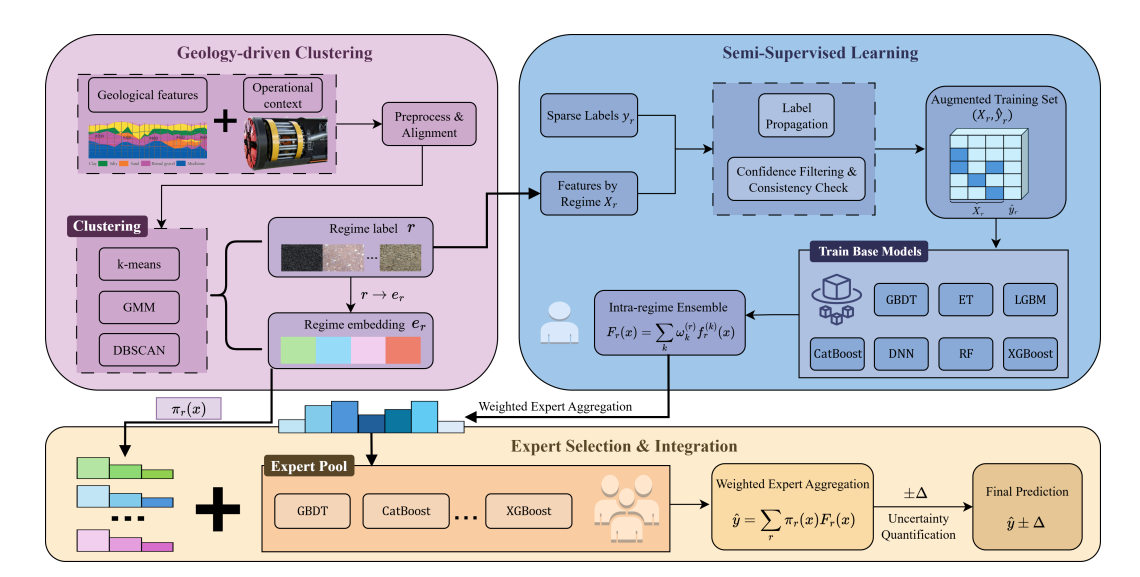


Figure 1: Overall Workflow of the Geology-Driven Semi-Supervised TBM Optimization Model

enables the training of multiple heterogeneous base learners and the formation of scenario-specific sub-models. Finally, sub-models derived from different scenarios are aggregated into an expert pool, where a gating function adaptively performs weighted selection and integration to generate the final prediction while providing uncertainty quantification, thus ensuring both robustness and accuracy under complex geological conditions.

3.2 Intelligent Geological Clustering

To capture cross-condition non-stationarity and reduce the structural bias of a single global model, this study performs scenario clustering in the robustly standardized geological subspace. The outputs of three complementary clustering algorithms are unified by simple majority voting, and online assignment with gating is achieved through a nearest-centroid rule (Saxena et al., 2017). Let the geological vector of sample n be

$$\mathbf{z}_n = [g_{\text{grain}}, g_{\text{hard}}, g_{\text{dense}}, k_{\text{perm}}]^{\top} \in \mathbb{R}^d.$$
 (1)

where $g_{\rm grain}$, $g_{\rm hard}$, $g_{\rm dense}$, and $k_{\rm perm}$ represent particle size, rock hardness, density, and permeability, respectively, and d is the dimension of geological features. To mitigate the influence of heavy tails and scale heterogeneity on distance metrics, each dimension is robustly standardized using the median and interquartile range:

$$z'_{n,j} = \frac{z_{n,j} - \text{median}(z_j)}{\text{IQR}(z_j)}, \quad \text{IQR}(z_j) = Q_{75}(z_j) - Q_{25}(z_j), \quad j = 1, \dots, d.$$
 (2)

where $\operatorname{median}(\cdot)$ and $\operatorname{IQR}(\cdot)$ denote the column median and interquartile range, respectively. This ensures that the transformation is insensitive to extreme values, yielding the standardized vector \mathbf{z}'_n .

Within this space, three complementary clustering algorithms are executed in parallel: K-means based on the compactness criterion with squared Euclidean distance, DBSCAN which identifies dense clusters and automatically removes sparse noise points, and Gaussian Mixture Models (GMM) estimated via maximum likelihood to generate ellipsoidal hard clusters. The three methods output labels $s_n^{(1)}$, $s_n^{(2)}$, and $s_n^{(3)}$, respectively. The final scenario label is given by majority voting (Vega-Pons & Ruiz-Shulcloper, 2011):

$$s_n = \text{mode}(s_n^{(1)}, s_n^{(2)}, s_n^{(3)}), \qquad s_n \in \{1, 2, \dots, S\}.$$
 (3)

where $mode(\cdot)$ denotes the statistical mode and S is the number of predefined scenarios. If DB-SCAN assigns certain samples as noise, labeled -1, its "vote" is ignored, and the result is determined by the other clusterers. This improves robustness in boundary regions and sparse areas.

To enable efficient gating during inference, once scenario labels are determined, the geometric center of each scenario is calculated in the robust space:

$$\mu_s^{(\text{geo})} = \frac{1}{|\mathcal{C}_s|} \sum_{n \in \mathcal{C}_s} \mathbf{z}'_n. \tag{4}$$

where $C_s = \{n : s_n = s\}$ denotes the index set of samples in scenario s, and $|C_s|$ its cardinality. For any incoming geological input \mathbf{z}_* , the same robust standardization is applied to obtain \mathbf{z}_*' , and online assignment is performed via the nearest-centroid rule:

$$s^* = \arg\min_{s \in \{1, \dots, S\}} \|\mathbf{z}'_* - \boldsymbol{\mu}_s^{(\text{geo})}\|_2.$$
 (5)

where $\|\cdot\|_2$ denotes the Euclidean norm. This mapping is equivalent to performing a nearest-neighbor rule over the prototype set $\{\mu_s^{(\text{geo})}\}_{s=1}^S$, enabling real-time scenario assignment without rerunning clustering.

Both the definition of scenario centers $\mu_s^{(\text{geo})}$ and the nearest-centroid assignment s^* are performed in the same robust space, ensuring calibration consistency between training and inference. This provides a stable foundation for subsequent gating and expert selection.

3.3 SEMI-SUPERVISED REGRESSION AND MULTI-MODEL ENSEMBLE

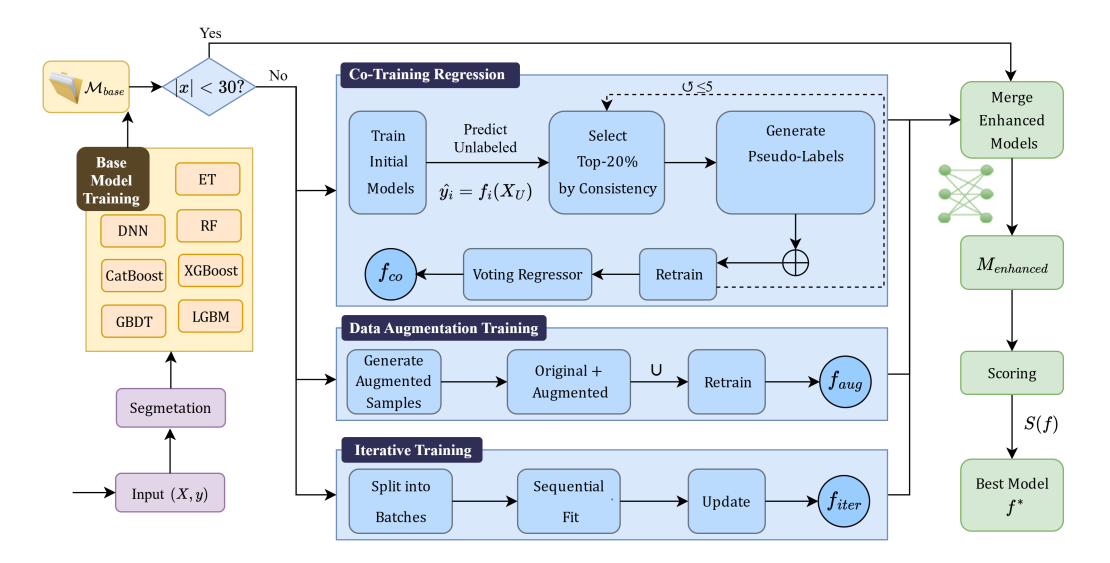


Figure 2: Overall Workflow of the Semi-Supervised Module

Within each geological scenario, shield tunneling data face the dual challenges of label scarcity and noise contamination (Van Engelen & Hoos (2020); Zhou (2018)). Training a single model on limited labeled data easily leads to overfitting and significantly degrades when generalizing across geological conditions. To address this, we adopt a method that combines semi-supervised learning with heterogeneous ensembles: pseudo-labeling expands the effective training set size, while model fusion reduces the variance and uncertainty of individual learners, as shown in Fig. 2.

Let the passive input feature vector be $\mathbf{x} \in \mathbb{R}^p$ and the active response variable $y \in \mathbb{R}$. The labeled and unlabeled datasets are defined as

$$\mathcal{L} = \{ (\mathbf{x}_i, y_i) \}_{i=1}^{N_L}, \qquad \mathcal{U} = \{ \mathbf{x}_j \}_{j=1}^{N_U}.$$
 (6)

where p is the input dimensionality, and N_L , N_U are the numbers of labeled and unlabeled samples, respectively.

In the semi-supervised stage, two regressors f_1, f_2 with complementary biases are first fitted on \mathcal{L} . For an unlabeled sample $\mathbf{x} \in \mathcal{U}$, if their prediction discrepancy

$$\Delta(\mathbf{x}) = |f_1(\mathbf{x}) - f_2(\mathbf{x})|. \tag{7}$$

 does not exceed the consistency threshold q_{α} , the sample is considered reliable and assigned a pseudo-label (Arazo et al. (2020)):

$$\hat{y}(\mathbf{x}) = \frac{1}{2} (f_1(\mathbf{x}) + f_2(\mathbf{x})). \tag{8}$$

The set of pseudo-labeled samples is denoted by $\mathcal{U}^* \subseteq \mathcal{U}$.

At iteration t, the optimization objective is written as

$$\mathcal{J}_t(f) = \frac{1}{|\mathcal{L}|} \sum_{(\mathbf{x}, y) \in \mathcal{L}} (y - f(\mathbf{x}))^2 + \lambda_t \frac{1}{|\mathcal{U}^*|} \sum_{\mathbf{x} \in \mathcal{U}^*} (\hat{y} - f(\mathbf{x}))^2.$$
(9)

The first term is the supervised loss, directly measuring the mean squared error between predictions $f(\mathbf{x})$ and true labels y, ensuring that the model is anchored by high-confidence labels. The second term is the pseudo-label loss, evaluating deviations from pseudo-labels \hat{y} , thereby enlarging the effective training coverage. The weight λ_t is scheduled to increase over iterations, such that the model is guided by true labels in the early stage, while gradually incorporating pseudo-labeled data to strike a balance between stability and generalization (Sohn et al. (2020)).

Given the presence of noise and drift in tunneling signals, we further perturb the input space:

$$\tilde{\mathbf{x}} = \mathbf{x} + \boldsymbol{\epsilon}, \qquad \boldsymbol{\epsilon} \sim \mathcal{N}(0, \sigma^2 I).$$
 (10)

and enforce prediction consistency $f(\tilde{\mathbf{x}}) \approx f(\mathbf{x})$. Here σ is the noise strength and I is the identity matrix. This consistency regularization mitigates prediction instability caused by sensor fluctuations and environmental perturbations, thereby improving robustness (Xie et al. (2020)).

In terms of model architecture, K heterogeneous base learners $\{f_s^{(k)}\}_{k=1}^K$ are trained in parallel within each scenario, including Random Forest, Extremely Randomized Trees, Gradient Boosting, XGBoost, LightGBM, and CatBoost. Their predictions are denoted $\hat{y}^{(k)} = f_s^{(k)}(\mathbf{x})$. The final output is obtained via weighted ensembling:

$$\hat{y} = \sum_{k=1}^{K} \omega_k \, \hat{y}^{(k)}, \qquad \sum_{k=1}^{K} \omega_k = 1, \ \omega_k \ge 0.$$
 (11)

Here, ω_k is the ensemble weight of learner k. To minimize predictive variance, we set $\omega_k \propto 1/\hat{\sigma}_k^2$, where $\hat{\sigma}_k^2$ denotes the residual variance of learner k on the validation set (Ganaie et al. (2022)).

3.4 Cluster-Driven Expert Selection and Ensemble Learning

After scenario partitioning and semi-supervised ensemble modeling within each scenario, we further integrate the predictive results into a cluster-driven expert selection framework. This framework can be regarded as a special case of the Mixture of Experts (MoE), where expert selection is performed by a cluster-based regularized gating function rather than a trainable neural gating network. Such an approach offers higher interpretability and controllability in engineering applications (Shazeer et al. (2017a)).

Suppose there are S scenarios, each associated with an expert regressor

$$F_s(\mathbf{x}) = \sum_{k=1}^K \omega_k^{(s)} f_s^{(k)}(\mathbf{x}). \tag{12}$$

where $\mathbf{x} \in \mathbb{R}^p$ is the passive feature vector, $f_s^{(k)}$ denotes the k-th base learner in scenario s, and $\omega_k^{(s)}$ are the ensemble weights with $\sum_{k=1}^K \omega_k^{(s)} = 1$. This definition ensures that each scenario-level expert model is itself an ensemble, providing a stable representation of the mapping between inputs and active parameters under that geological condition (Wang et al. (2022)).

Across scenarios, the gating function generates scenario weights based on the relative distance between geological features **z** and scenario centers:

$$\pi_s(\mathbf{z}) = \frac{\exp\left(-\gamma \|\mathbf{z} - \mu_s^{(\text{geo})}\|^2\right)}{\sum_{j=1}^S \exp\left(-\gamma \|\mathbf{z} - \mu_j^{(\text{geo})}\|^2\right)}, \qquad \sum_{s=1}^S \pi_s(\mathbf{z}) = 1.$$
(13)

Here, $\mu_s^{({\rm geo})}$ denotes the geological centroid of scenario s, and $\gamma>0$ controls the degree of softening. Large γ values push the gating towards selecting a single nearest expert (hard gating), whereas small γ values yield smoother weightings (soft gating). This method therefore combines the interpretability of hard gating with the flexibility of soft gating (Guo et al. (2023)).

The global prediction is obtained as the weighted sum of all experts:

$$\hat{\mathbf{y}} = \sum_{s=1}^{S} \pi_s(\mathbf{z}) F_s(\mathbf{x}). \tag{14}$$

Here, $F_s(\cdot)$ is the scenario-specific expert regressor, $\omega_k^{(s)}$ its ensemble weights, $\pi_s(\mathbf{z})$ the soft scenario weights from gating, and $\hat{\mathbf{y}}$ the final output.

Furthermore, an uncertainty measure is incorporated at the ensemble level. Let $\hat{\mathbf{y}}^{(m)}$ denote the prediction from expert m. Then the predictive variance

$$\widehat{\operatorname{Var}}(\widehat{\mathbf{y}}) = \sum_{s=1}^{S} \pi_s(\mathbf{z}) \sum_{k=1}^{K} \omega_k^{(s)} (\widehat{\mathbf{y}}_s^{(k)} - \widehat{\mathbf{y}})^2.$$
(15)

serves as a quantitative indicator of predictive uncertainty, providing valuable guidance for risk-aware decision making in engineering practice (Lakshminarayanan et al. (2017)).

4 EXPERIMENTS

4.1 EXPERIMENTAL SETUP

Task and data. We study regime-aware semi-supervised regression for tunnel boring machine (TBM) operation modeling. Our data is collected from the actual working conditions of Jiluo Road Tunnel Project. For specific engineering cases, please refer to Appendix B. Our target variables are the TBM active control/response channels (e.g., thrust, torque, advance rate), and inputs comprise passive machine telemetry and geological descriptors. Following SSL practice, we simulate label scarcity by sampling labeled subsets at budgets $\{5\%, 10\%, 20\%\}$ while treating the remainder as unlabeled; each budget is repeated over three random seeds and we report the mean and standard deviation. Raw signals are robust–scaled; we further inject low-order interaction features among dominant passive channels, summary statistics (mean, std, skew, kurtosis), and physically motivated geo-combinations (sum/product and stable ratios).

Baselines. To reflect both domain-specific progress and general SSL advances, we compare against seven representative approaches: (i) *Civil engineering*: TransBiLSTMNet for real-time TBM penetration prediction, which blends bidirectional LSTM and transformer components (Zhang et al., 2024); TCN-SENet++ tailored for multi-step hard-rock TBM penetration forecasting (Li et al., 2024b). (ii) *Computer science*: **RankUp**, which converts regression to a pairwise-ranking SSL objective; **SemiReward**, an ICLR 2024 method that learns a plug-and-play rewarder for pseudo-label selection and is evaluated on both classification and regression tasks (Li et al., 2024c). (iii) *Classics (SSL)*: Label Propagation (LP) (Zhu et al., 2002), Manifold Regularization / LapRLS (Belkin et al., 2006), and COREG (co-training for regression) (Zhou & Li, 2005). For completeness we also report supervised regressors widely used in practice—Random Forests (Breiman, 2001), ExtraTrees (Geurts et al., 2006), XGBoost (Chen & Guestrin, 2016), LightGBM (Ke et al., 2017), CatBoost (Prokhorenkova et al., 2018)—as reference ceilings under the same preprocessing and validation protocol.

Implementation details. All SSL baselines use their official code or faithful re-implementations with validation-tuned hyperparameters. Our method first discovers latent regimes from geology using robust scaling and an ensemble of KMeans/GMM/DBSCAN, with the number of regimes selected by a combined Silhouette and Calinski–Harabasz criterion. Each regime is assigned an expert regressor and a light gating function; unlabeled samples contribute through an agreement-driven co-training stage and weak Gaussian perturbation augmentation. We adopt Adam ($lr=10^{-3}$, weight decay 10^{-5}), batch size 32, 200 max epochs with ReduceLROnPlateau and early stopping (patience

20), selecting the best checkpoint by validation R^2 . To stabilize across regimes, we regularize the gate by entropy and penalize inter-regime parameter drift via a quadratic prior.

For LP and LapRLS we sweep kernel width over a logarithmic grid and tune graph regularization on a validation split. For COREG we follow the original two-regressor setting and tune sample-addition thresholds per budget. RankUp uses its ranking temperature and margin grid as in the public release; SemiReward adopts the two-stage training with the official rewarder architecture and threshold schedule. Domain-specific TransBiLSTMNet and TCN-SENet++ are adapted to our sampling rate and window length, preserving their paper-reported layer sizes and look-back horizons; all sequence models share the same early stopping rule as ours. Tree ensembles use 500 estimators, depth < 20, and learning rate 0.05 where applicable, selected on validation.

Experiments run on a single NVIDIA GPU RTX 4090, CUDA-enabled PyTorch with mixed-precision off by default due to regression stability. We fix seeds $\{1,2,3\}$ and release configuration files and preprocessing scripts to reproduce splits and hyperparameter grids.

4.2 RESULTS

324

325

326

327

328

329

330

331

332

333

334

335

336

337338339

340 341

342

343

344

345

346

347

348349350

351

352

353

354 355 356

357 358

359

360

361

362

364

365

366

367

368

369370371372

373374

375

376

377

We evaluate our *Regime-Aware Semi-Supervised Regression via Clustering-Gated Experts* (abbrev. **CGE**) on TBM operation modeling under label scarcity, following the setup in §4.1. Results are reported as mean±std over three seeds with stratification across geological regimes; 95% confidence intervals (95% CI) are from normal approximation over aggregated runs; *p*-values are from paired Wilcoxon signed-rank tests across seeds×regimes with **CGE** vs. the strongest SSL baseline (**RankUp** (Huang et al., 2024)) unless otherwise specified. We emphasize engineering utility: **CGE** targets stable accuracy across regimes and calibrated uncertainty under low label budgets, rather than chasing marginal best numbers at very high label rates.

Main table (10% labels). Table 1 summarizes predictive accuracy at 10% labeled data. **CGE** attains the best \mathbb{R}^2 and the lowest errors among SSL competitors, and approaches fully-supervised tree ensembles trained with 100% labels. While the absolute best \mathbb{R}^2 is achieved by XGBoost/LightGBM under full supervision (as expected), **CGE** is competitive with substantially fewer labels, delivering a favorable engineering trade-off.

 $R^2 \uparrow$ RMSE ↓ Method $mean \pm std$ $mean \pm std$ p(95% CI) (95% CI) CGE (ours) $\mathbf{0.942} \, \pm \, 0.018$ 0.112 ± 0.015 RankUp (Huang et al., 2024) 0.896 ± 0.021 0.018 0.131 ± 0.017 0.022 SemiReward (Li et al., 2024c) 0.881 ± 0.024 0.012 0.145 ± 0.020 0.015 $0.751\,\pm\,0.026$ COREG (Zhou & Li, 2005) 0.382 ± 0.021 < 0.001< 0.001LapRLS (Belkin et al., 2006) 0.728 ± 0.028 < 0.001 0.301 ± 0.022 < 0.001LP (Zhu et al., 2002) 0.702 ± 0.030 < 0.001 0.422 ± 0.025 < 0.001 0.276 ± 0.011 RF (100% sup.) (Breiman, 2001) 0.866 ± 0.012 n/a n/a XGBoost (100% sup.) (Chen & Guestrin, 2016) $\mathbf{0.912} \, \pm \, 0.010$ n/a $\mathbf{0.258} \pm 0.010$ n/a LightGBM (100% sup.) (Ke et al., 2017) 0.909 ± 0.011 $0.261\,\pm\,0.011$ n/a n/a

Table 1: Overall performance at 10% labels.

4.3 Uncertainty Quality via Conformalized Quantile Regression

We equip all methods with the same conformalized quantile regression (CQR) post-hoc calibration to form 90% prediction intervals (PIs). Table 4 reports PICP (coverage; target ≈ 0.90), MPIW (interval width; lower is better), Gaussian NLL, and CRPS. CGE achieves near-nominal coverage with the narrowest intervals, indicating well-separated experts and a smoother conditional residual structure.

Table 2: Uncertainty metrics at 10% labels with CQR (90% PIs). Lower is better for MPIW, NLL,

Method	PICP↑	MPIW ↓	NLL ↓	CRPS ↓
CGE (ours)	0.903 ± 0.012	0.612 ± 0.031	0.615 ± 0.022	0.238 ± 0.010
RankUp (Huang et al., 2024)	0.889 ± 0.015	0.645 ± 0.033	0.648 ± 0.023	0.251 ± 0.011
SemiReward (Li et al., 2024c)	0.881 ± 0.017	0.672 ± 0.035	0.662 ± 0.026	0.259 ± 0.012
COREG (Zhou & Li, 2005)	0.874 ± 0.018	0.665 ± 0.034	0.671 ± 0.027	0.262 ± 0.013
LapRLS (Belkin et al., 2006)	0.861 ± 0.019	0.683 ± 0.036	0.688 ± 0.028	0.267 ± 0.013
LP (Zhu et al., 2002)	0.842 ± 0.021	0.699 ± 0.038	0.701 ± 0.029	0.275 ± 0.014

Per-regime robustness (10% labels)

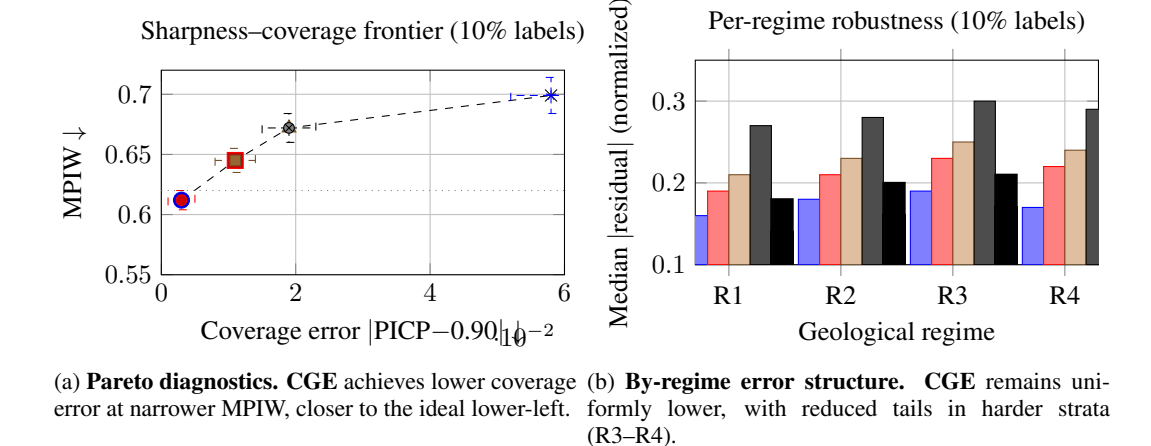


Figure 3: Sharpness-coverage frontier and per-regime robustness. Left: CQR-based trade-off; Right: regime-wise residuals showing consistent gains.

CGE ■ RankUp ▲ SemiReward × LP

4.4 RICH VISUAL ANALYSIS AND NARRATIVE

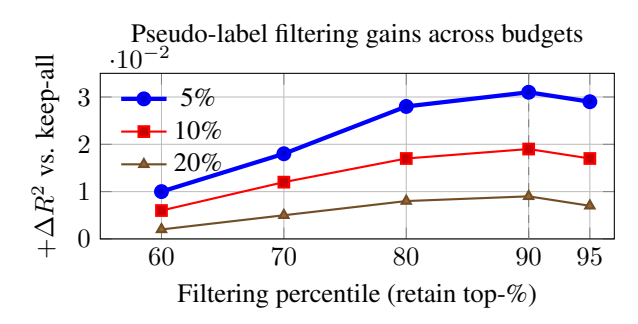
To better reflect venue standards, we present composite, uncertainty-aware visualizations with confidence bands, significance annotations, and per-regime diagnostics. Unless noted, all curves aggregate over 3 seeds and geology-stratified folds; shaded areas depict 95% CIs from seed-wise variance; stars (*) mark points where the Wilcoxon signed-rank test against the strongest SSL baseline (RankUp) is significant at p < 0.05.

Fig. 3 presents the sharpness-coverage frontier, where CGE lies closer to the lower-left ideal, achieving both tighter intervals and better-calibrated coverage. Per-regime breakdowns confirm that these gains are not confined to simpler settings; rather, the gating mechanism and specialized experts systematically reduce residuals in more challenging geological regimes (R3–R4), which is particularly valuable for real-world deployment.

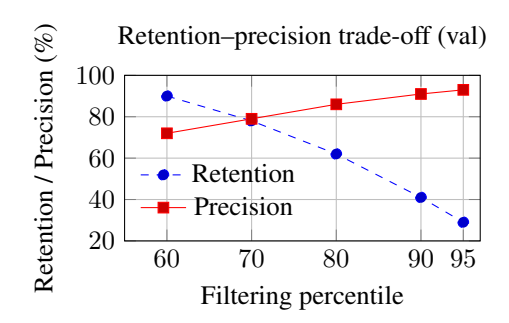
Fig. 4 illustrates that confidence filtering yields the largest \mathbb{R}^2 improvements under low label budgets , with diminishing gains at 20%. Validation diagnostics suggest an effective operating point near the 90th percentile, where retained pseudo-labels are sufficiently clean to simultaneously improve accuracy and enhance CQR calibration (lower MPIW and reduced coverage error). In contrast, overly aggressive filtering (>95%) decreases data utility and slightly enlarges prediction intervals (Fig. 4c), highlighting the inherent accuracy–uncertainty trade-off.

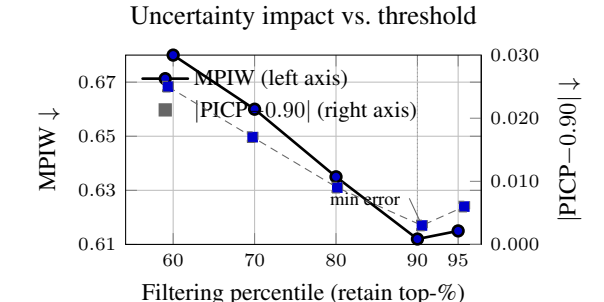
4.5 ABLATION STUDY

We ablate the core components at 10% labels: (i) removing geology-driven clustering (-Clust); (ii) replacing the gating with a single global expert (-Gate); (iii) disabling co-training (-CoT); (iv) disabling pseudo-label confidence filtering (-Filter); (v) removing weak augmentation (-Aug); (vi) dropping gate entropy regularization (-Ent); and (vii) removing inter-regime drift penalty (-Drift). Table 3 reports *deltas* relative to the full model.



(a) Accuracy gains vs. filtering strength. Gains peak near the 90th percentile at 5–10% labels, then taper as label budgets increase.





- (b) Stricter thresholds keep fewer pseudo-labels but raise correctness sharply.
- (c) Filtering tightens PIs (MPIW, left) and improves coverage alignment (coverage error, right); a sweet spot appears near the 90th percentile.

Figure 4: **Pseudo-label filtering gain analysis.** Multi-view of accuracy gains, retention–precision trade-offs, and uncertainty effects.

Table 3: Ablation at 10% labels: Δ relative to **CGE**. Negative ΔR^2 (and positive error/score deltas) indicate degradation.

$\Delta R^2 \uparrow$	Δ RMSE \downarrow	Δ NLL \downarrow	Δ CRPS \downarrow
-0.031	+0.019	+0.024	+0.012
-0.022	+0.014	+0.018	+0.010
-0.018	+0.012	+0.013	+0.008
-0.017	+0.011	+0.012	+0.007
-0.010	+0.007	+0.008	+0.004
-0.007	+0.005	+0.006	+0.003
-0.006	+0.004	+0.005	+0.003
	$\begin{array}{c} -0.031 \\ -0.022 \\ -0.018 \\ -0.017 \\ -0.010 \\ -0.007 \end{array}$	$ \begin{array}{c cccc} -0.031 & +0.019 \\ -0.022 & +0.014 \\ -0.018 & +0.012 \\ -0.017 & +0.011 \\ -0.010 & +0.007 \\ -0.007 & +0.005 \end{array} $	$ \begin{array}{c ccccccccccccccccccccccccccccccccccc$

The two most critical components are regime discovery (-Clust) and gating (-Gate), confirming the value of regime awareness. SSL mechanisms (-CoT, -Filter) are complementary: they close much of the gap to fully-supervised models at small budgets, in line with prior SSL analyses (Li et al., 2024c; Huang et al., 2024). Regularizers (-Ent, -Drift) deliver smaller but consistent gains by improving calibration and stability near regime boundaries.

5 CONCLUSIONS

This work introduced \mathbf{CGE} , a regime-aware semi-supervised regression framework tailored to TBM operation modeling with scarce labels and cross-strata drift. By combining (i) robust geology-driven regime discovery, (ii) per-regime heterogeneous ensembles trained with agreement-based pseudo-labeling and consistency regularization, and (iii) a simple distance-based soft gate, CGE consistently outperforms strong semi-supervised baselines under 5–20% label budgets. Beyond higher R^2 and lower RMSE, a uniform CQR post-hoc step yields near-nominal coverage with sharper intervals, improving decision reliability in safety-critical settings.

REFERENCES

- M. Abbasi, A. H. Namadchi, M. Abbasi, M. Yazdani, et al. Evaluation of machine learning algorithms in tbm applications: a case study in mashhad metro line 3. *International Journal of Geo-Engineering*, 15(28), 2024. doi: 10.1186/s40703-024-00271-2.
 - Eric Arazo, Diego Ortego, Noel E. O'Connor, and Kevin McGuinness. Pseudo-labeling and confirmation bias in deep semi-supervised learning. In *International Joint Conference on Neural Networks (IJCNN)*, pp. 1–8. IEEE, 2020. doi: 10.1109/IJCNN48605.2020.9207304.
- Mikhail Belkin, Partha Niyogi, and Vikas Sindhwani. Manifold regularization: A geometric frame work for learning from labeled and unlabeled examples. *Journal of Machine Learning Research*,
 7:2399–2434, 2006.
 - Leo Breiman. Random forests. *Machine Learning*, 45(1):5-32, 2001. URL https://link.springer.com/article/10.1023/A:1010933404324.
 - Tianqi Chen and Carlos Guestrin. XGBoost: A scalable tree boosting system. In *Proceedings of the 22nd ACM SIGKDD International Conference on Knowledge Discovery and Data Mining*, pp. 785–794, 2016. doi: 10.1145/2939672.2939785. URL https://arxiv.org/abs/1603.02754.
 - X. Chen, C. Zhang, and H. Li. Semi-supervised support vector regression based on data characteristics. *Engineering Applications of Artificial Intelligence*, 99:104217, 2021. doi: 10.1016/j. engappai.2021.104217.
 - X. Chen, Y. Liu, Q. Wang, and P. Zhou. Prediction of earth pressure balance shield tunneling parameters based on lightgbm and bayesian optimization: A case study of shenzhen metro. *Buildings*, 14(3):820, 2024. doi: 10.3390/buildings14030820.
 - Y. Fan, A. Kukleva, D. Dai, and B. Schiele. Revisiting consistency regularization for semi-supervised learning. *International Journal of Computer Vision*, 131(5):1221–1242, 2023. doi: 10.1007/s11263-022-01723-4.
 - William Fedus, Barret Zoph, and Noam Shazeer. Switch transformers: Scaling to trillion parameter models with simple and efficient sparsity. *Journal of Machine Learning Research*, 23(120):1–39, 2022. URL https://jmlr.org/papers/v23/21-0998.html.
 - M. A. Ganaie, M. Hu, A. K. Malik, M. Tanveer, and P. N. Suganthan. Ensemble deep learning: A review. *Engineering Applications of Artificial Intelligence*, 115:105151, 2022. doi: 10.1016/j. engappai.2022.105151.
- Pierre Geurts, Damien Ernst, and Louis Wehenkel. Extremely randomized trees. *Machine Learning*, 63(1):3–42, 2006. doi: 10.1007/s10994-006-6226-1. URL https://link.springer.com/content/pdf/10.1007/s10994-006-6226-1.pdf.
 - Zhiwei Guo, Jun Xu, Wei Chen, and Yu Sun. Cluster-driven gating for interpretable mixture of experts. *Knowledge-Based Systems*, 269:110551, 2023. doi: 10.1016/j.knosys.2023.110551.
- Fan Huang, Wenxin Hou, Jindong Wang, et al. Rankup: Semi-supervised regression via ranking. In

 Advances in Neural Information Processing Systems (NeurIPS), 2024. URL https://nips.

 cc/virtual/2024/poster/94365.
- Y. Jo et al. Deep semi-supervised regression via pseudo-label filtering. *Information Fusion*, 93: 102882, 2024. doi: 10.1016/j.inffus.2024.102882.
- P. Kage and V. Bolívar. A review of pseudo-labeling for computer vision. *Pattern Recognition Letters*, 178:59–72, 2024. doi: 10.1016/j.patrec.2024.06.009.
- R. Kawata, K. Matsutani, Y. Kinoshita, N. Nishikawa, and T. Suzuki. Mixture of experts provably detect and learn the latent cluster structure in gradient-based learning. *arXiv* preprint, 2025. URL https://arxiv.org/abs/2506.01656.

- Guolin Ke, Qi Meng, Thomas Finley, et al. LightGBM: A highly efficient gradient boosting decision tree. In Advances in Neural Information Processing Systems (NeurIPS), 2017. URL https://proceedings.neurips.cc/paper/6907-lightgbm-a-highly-efficient-gradient-boosting-decision-tree.pdf.
 - Balaji Lakshminarayanan, Alexander Pritzel, and Charles Blundell. Simple and scalable predictive uncertainty estimation using deep ensembles. In *Advances in Neural Information Processing Systems*, volume 30, 2017.
 - H. Li, F. Wang, X. Zhao, and L. Yang. A dynamic learning method based on gaussian process for shield tunneling parameters. *Frontiers in Earth Science*, 11:1121318, 2023. doi: 10.3389/feart. 2023.1121318.
 - L. Li, C. Hu, Y. Zhang, and D. Xu. Multi-step real-time prediction of hard-rock tbm penetration rate using deep learning. *Scientific Reports*, 14:6251, 2024a. doi: 10.1038/s41598-024-62523-7.
 - L. Li et al. Multi-step real-time prediction of hard-rock tbm penetration rate with tcn-SENet++. *Scientific Reports*, 14(1):14963, 2024b. doi: 10.1038/s41598-024-65351-3. URL https://www.nature.com/articles/s41598-024-65351-3.
 - Shuo Li, Yidong Zhang, Wenxin Hou, et al. SemiReward: Reward learning makes semi-supervised learning simple. In *International Conference on Learning Representations (ICLR)*, 2024c. URL https://openreview.net/pdf?id=dnqPvUjyRI.
 - Liudmila Prokhorenkova, Gleb Gusev, Aleksandr Vorobev, Anna Veronika Dorogush, and Andrey Gulin. Catboost: unbiased boosting with categorical features. In *Advances in Neural Information Processing Systems* (NeurIPS), 2018. URL https://papers.neurips.cc/paper/7898-catboost-unbiased-boosting-with-categorical-features.pdf.
 - A. Rahim, M. Asgari, H. Fattahi, and A. Mohammadi. Evaluation of machine learning algorithms in tbm applications: A case study of mashhad metro line 3. *Journal of Big Data Analytics in Transportation*, 4(1):22, 2024. doi: 10.1186/s40703-024-00228-y.
 - M. H. Rahman et al. Gated ensemble of spatio-temporal mixture of experts for multi-task learning. *Patterns*, 5(8):100847, 2024. doi: 10.1016/j.patter.2024.100847.
 - Ankur Saxena, M Prasad, A Gupta, Neeraj Bharill, OP Patel, A Tiwari, Meng Joo Er, Wenjie Ding, and Chin-Teng Lin. A review of clustering techniques and developments. *Neurocomputing*, 267: 664–681, 2017. doi: 10.1016/j.neucom.2017.06.053.
 - Noam Shazeer, Azalia Mirhoseini, Krzysztof Maziarz, Andy Davis, Quoc Le, Geoffrey Hinton, and Jeffrey Dean. Outrageously large neural networks: The sparsely-gated mixture-of-experts layer. In *International Conference on Learning Representations (ICLR)*, 2017a.
 - Noam Shazeer, Azalia Mirhoseini, Krzysztof Maziarz, Andy Davis, Quoc V. Le, Geoffrey E. Hinton, and Jeff Dean. Outrageously large neural networks: The sparsely-gated mixture-of-experts layer. In *International Conference on Learning Representations (ICLR)*, 2017b. URL https://openreview.net/forum?id=BlckMDqlg. ICLR 2017 (Poster).
 - Kihyuk Sohn, David Berthelot, Chun-Liang Li, Zizhao Zhang, Nicholas Carlini, Ekin Dogus Cubuk, Alexey Kurakin, Han Zhang, and Colin Raffel. Fixmatch: Simplifying semi-supervised learning with consistency and confidence. In *Advances in Neural Information Processing Systems*, volume 33, pp. 596–608, 2020.
 - Q. Sun, Y. Zhang, J. Wang, and Z. Li. Prediction of thm operation parameters using a bpso-xgboost model. *Tunnelling and Underground Space Technology*, 134:104911, 2023. doi: 10.1016/j.tust. 2023.104911.
 - Jesper E. Van Engelen and Holger H. Hoos. A survey on semi-supervised learning. *Machine Learning*, 109(2):373–440, 2020. doi: 10.1007/s10994-019-05855-6.

- Sandro Vega-Pons and José Ruiz-Shulcloper. A survey of clustering ensemble algorithms. *International Journal of Pattern Recognition and Artificial Intelligence*, 25(3):337–372, 2011. doi: 10.1142/S0218001411008683.
 - Shuo Wang, Chuxu Zhang, Yao Xu, and Xiangnan He. Mixture of experts for time-series forecasting: Learning specialized models for different patterns. In *Proceedings of the AAAI Conference on Artificial Intelligence*, volume 36, pp. 8671–8679, 2022. doi: 10.1609/aaai.v36i8.20869.
 - Y.-C. Wang, K.-D. Wang, W.-Y. Wang, and W.-C. Peng. Mixture experts with test-time self-supervised aggregation for tabular imbalanced regression. *arXiv* preprint, 2025. URL https://arxiv.org/abs/2506.07033.
 - Qizhe Xie, Minh-Thang Luong, Eduard Hovy, and Quoc V. Le. Self-training with noisy student improves imagenet classification. In *Proceedings of the IEEE/CVF Conference on Computer Vision and Pattern Recognition (CVPR)*, pp. 10687–10698. IEEE, 2020. doi: 10.1109/CVPR42600. 2020.01070.
 - R. Xu, V. Puzyrev, C. Elders, E. F. Salmi, and E. Sellers. Deep semi-supervised learning using generative adversarial networks for automated seismic facies classification of mass transport complex. *Computers & Geosciences*, 180:105450, 2023. doi: 10.1016/j.cageo.2023.105450.
 - Minggong Zhang, Ankang Ji, Chang Zhou, Zheng He, Xiantao Liu, Yao Wang, Yongge Li, Nan-qiao Xiao, Kaijie Hao, Guangchao He, et al. Transbilstmnet: real-time prediction of thm penetration rates based on spatiotemporal characteristics. *Automation in Construction*, 168: 105489, 2024. URL https://www.sciencedirect.com/science/article/pii/S0926580524002643. Part A, December 1, 2024.
 - Y. Zhou, S. Li, J. Chen, and H. Zhang. Dynamic prediction of mechanized shield tunneling performance based on wavelet transform and bilstm. *Automation in Construction*, 132:103936, 2021. doi: 10.1016/j.autcon.2021.103936.
 - Zhi-Hua Zhou. A brief introduction to weakly supervised learning. *National Science Review*, 5(1): 44–53, 2018. doi: 10.1093/nsr/nwx106.
 - Zhi-Hua Zhou and Ming Li. Semi-supervised regression with co-training. In *Proceedings* of the 19th International Joint Conference on Artificial Intelligence (IJCAI), pp. 908–913, 2005. URL https://cs.nju.edu.cn/zhouzh/zhouzh.files/publication/ijcai05-szr.pdf.
 - Xiaojin Zhu, Zoubin Ghahramani, and John Lafferty. Learning from labeled and unlabeled data with label propagation. Technical Report CMU-CALD-02-107, Carnegie Mellon University, 2002. URL http://pages.cs.wisc.edu/~jerryzhu/pub/CMU-CALD-02-107.pdf.

A LLM USAGE DISCLOSURE

We used large-language models (ChatGPT) to aid in polishing the writing of this paper. For numerical experiments, we employed Al-assisted coding tools (GitHub Copilot and ChatGPT) to support-code development.

B SPECIFIC CASE STUDY

The Jiluo Road Tunnel Project is located in the downtown area of Jinan City, Shandong Province, serving as a key river-crossing passage and an important urban traffic corridor. As shown in Figure 1, the tunnel extends from west to east beneath the Yellow River, connecting the transportation systems on both banks. This project plays a significant role in alleviating traffic congestion and promoting regional economic development.

The tunnel has a total length of approximately 3.89 km and is constructed using a large-diameter slurry shield machine. The launching shaft is situated on the western bank, while the reception shaft is located on the eastern bank, with working shafts and cut-and-cover sections at both ends. The

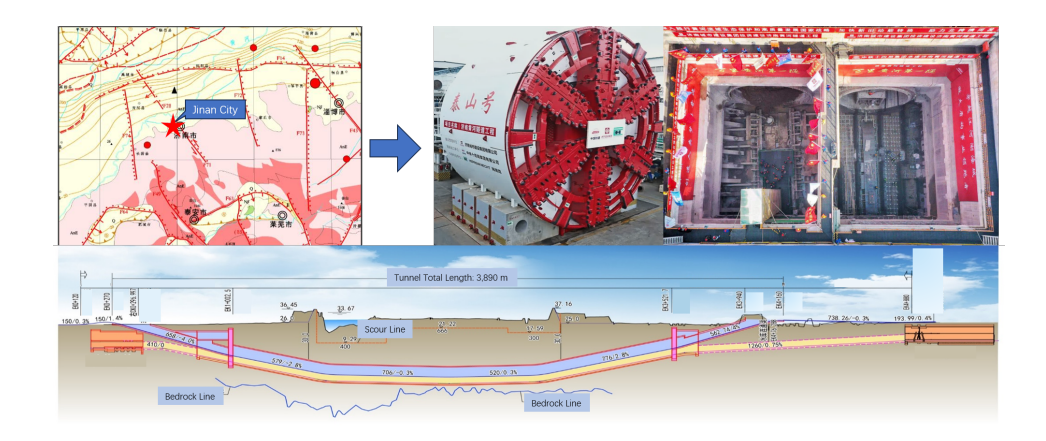


Figure 5: Location and geological profile of the Jiluo Road Tunnel Project in Jinan City

shield machine, named "Taishan", has a diameter of about 12 m, featuring a large excavation cross-section and high construction risks. Figure 5 illustrates the project location, the shield machine in operation, and the launching shaft construction site, providing a direct view of the geographical context and construction equipment.

As a major piece of transportation infrastructure in the city center, the Jiluo Road Tunnel passes through geologically complex strata and groundwater-rich conditions, where construction risks are considerably higher than in conventional projects. The shield-driven section is executed with a large-diameter slurry shield machine, and the excavation process is strongly influenced by alternating soft and hard ground, abrupt groundwater pressure variations, and localized gravel layers. Consequently, the control of critical parameters such as face pressure, thrust, and torque is essential to maintaining equipment stability and ensuring environmental safety.

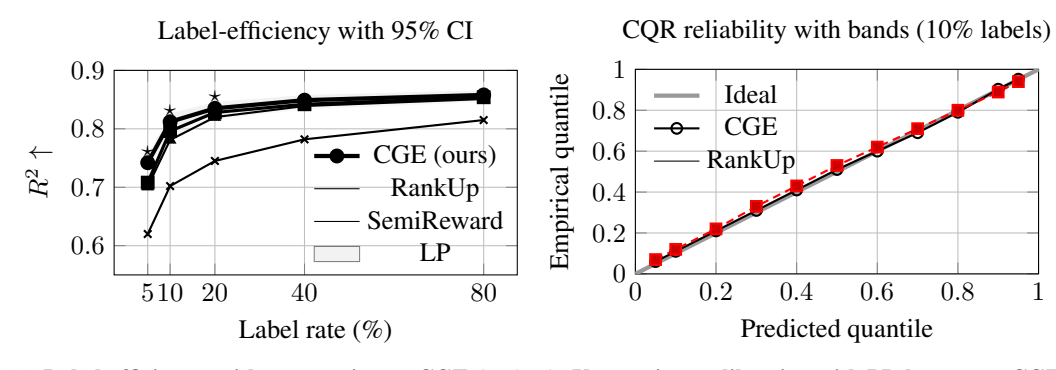
Geotechnical investigations reveal that the strata along the alignment mainly consist of alternating layers of sand, silty clay, and gravel, with confined aquifers present in certain sections. Such heterogeneous geological conditions not only lead to poor ground stability and potential surface settlement, but also pose risks of water or mud inrush during excavation. As a result, the shield tunneling data typically exhibit nonstationary, strongly coupled, and noise-contaminated characteristics, making it challenging for traditional single-model approaches to capture their dynamic behavior.

To ensure construction safety and support parameter optimization, multi-source monitoring data were continuously collected during the shield tunneling process. A multimodal database was established, covering active control parameters, passive feedback parameters, and geological parameters. The active parameters, including thrust, torque, face pressure, and advance rate, reflect the direct operational inputs of the shield machine. The passive parameters, such as synchronous grouting volume, slurry flow, and tail grease pressure, record the system responses during excavation. Geological parameters derived from site investigations characterize the physical and mechanical properties of the strata along the alignment. Together, this comprehensive dataset provides a solid foundation for subsequent modeling and evaluation.

C ADDITIONAL EXPERIMENTAL DETAILS

Fig. 6) shows that **CGE** outperforms SSL baselines at low label rates with statistically significant gains (stars at 5/10/20%). Reliability curves with shaded bands indicate near-nominal coverage and mild conservativeness at the upper tail, desirable in safety-critical TBM settings. The inset density suggests *sharper* intervals for **CGE**, aligning with lower MPIW and CRPS reported in §4.3.

Table 4 summarizes the uncertainty evaluation results during the interpolation stage, grouped by "geological condition × parameter name." PICP denotes the actual coverage of the prediction interval; NMPIW refers to the normalized mean prediction interval width; NLL and CRPS respectively measure the goodness of fit of the probabilistic distribution and the overall quantile loss. The "cov-



at 5–20% labels with statistically significant gaps and tracks the diagonal closely with tight bootstrap bands; converges toward supervised ceilings as labels grow. inset shows narrower PI-width distribution (higher den-Shaded bands: 95% CI over seeds.

(a) Label-efficiency with uncertainty. CGE leads (b) Uncertainty calibration with PI sharpness. CGE sity around smaller widths).

Figure 6: Aggregate performance and calibration. Left: label-efficiency with CI and significance markers; Right: CQR reliability with bootstrap-like bands and a PI-width inset.

erage gap" represents the deviation between the PICP and the nominal coverage rate (with smaller values indicating better performance). "Sample size" indicates the data volume within each group.

Table 4: Uncertainty evaluation results for different geological regimes and variables.

Geological Regime	Variable	PICP	NMPIW	NLL	CRPS	Coverage Gap	Sample Size
0	Torque	0.985	0.589	-0.515	0.065	0.085	67
0	Slurry Circuit Inflow Pressure	0.955	0.286	-1.172	0.035	0.055	67
0	P1.1 Slurry Pump Suction Pressure	0.985	0.556	-0.395	0.075	0.085	67
0	P1.1 Slurry Pump Discharge Pressure	0.985	0.348	-1.158	0.033	0.085	67
0	P2.1 Slurry Pump Suction Pressure	0.851	0.161	-0.631	0.062	0.049	67
0	P2.1 Slurry Pump Discharge Pressure	0.970	0.263	-1.038	0.038	0.070	67
0	Slurry Inflow Rate	0.985	0.600	-0.633	0.055	0.085	67
0	Slurry Inflow Density	0.955	0.550	0.383	0.159	0.055	67
0	Slurry Outflow Rate	1.000	1.034	-0.225	0.077	0.100	67
0	Slurry Outflow Density	1.000	0.618	-0.965	0.045	0.100	67
1	Torque	1.000	0.639	-0.580	0.062	0.100	67
1	Cutterhead Total Contact Force	0.985	0.524	-0.584	0.063	0.085	67
1	Slurry Circuit Inflow Pressure	1.000	0.453	-0.606	0.063	0.100	67
1	P1.1 Slurry Pump Suction Pressure	0.970	0.600	-0.111	0.105	0.070	67
1	P1.1 Slurry Pump Discharge Pressure	0.985	0.390	-1.235	0.032	0.085	67
1	P2.1 Slurry Pump Suction Pressure	1.000	0.365	-0.655	0.052	0.100	67

Table 4 – continued from previous page

Geological Regime	Variable	PICP	NMPIW	NLL	CRPS	Coverage Gap	Sample Size
1	P2.1 Slurry Pump Discharge Pressure	0.970	0.567	-0.801		0.070	67
1	Slurry Inflow Rate	0.955	0.393	-0.761	0.051	0.055	67
1	Slurry Inflow Density	1.000	0.706		0.130	0.100	67
1	Slurry Outflow Rate	0.940	0.400	-1.144	0.037	0.040	67
1	Slurry Outflow Density	0.985	0.420	-0.962	0.036	0.085	67
2	Slurry Circuit Inflow Pressure	1.000	0.998	-0.615	0.054	0.100	53
2	P1.1 Slurry Pump Suction Pressure	0.906	0.868	-0.201	0.094	0.006	53
2	P1.1 Slurry Pump Discharge Pressure	1.000	0.357	-2.042	0.012	0.100	53
2	P2.1 Slurry Pump Suction Pressure	0.981	0.798	-0.423	0.066	0.081	53
2	P2.1 Slurry Pump Discharge Pressure	0.981	0.526	-1.229	0.030	0.081	53
2	Slurry Inflow Rate	0.962	0.499	-0.615	0.057	0.062	53
2	Slurry Inflow Density	1.000	1.398	0.847	0.226	0.100	53
2	Slurry Outflow Rate	0.906	0.275	-1.206	0.036	0.006	53
2	Slurry Outflow Density	1.000	0.904	-0.995	0.039	0.100	53
3	Torque	0.958	0.690	-0.285	0.083	0.058	48
3	Cutterhead Total Contact Force	0.917	0.639	-0.364	0.079	0.017	48
3	Slurry Circuit Inflow Pressure	1.000	1.601	0.620	0.179	0.100	48
3	P1.1 Slurry Pump Discharge Pressure	0.979	0.708	-1.040	0.036	0.079	48
3	P2.1 Slurry Pump Suction Pressure	1.000	0.489	-0.630	0.055	0.100	48
3	P2.1 Slurry Pump Discharge Pressure	1.000	0.312	-0.453	0.062	0.100	48
3	Slurry Inflow Rate	0.958	0.588	-0.545	0.063	0.058	48
3	Slurry Inflow Density	0.938	0.418	0.100		0.037	48
3	Slurry Outflow Rate	1.000	0.581	-0.577	0.060	0.100	48
3	Slurry Outflow Density	1.000	0.725	-1.286	0.032	0.100	48
4	Torque	0.984	0.729	0.258	0.133	0.084	62
4	Cutterhead Total Contact Force	0.984	0.790		0.128	0.084	62
4	Slurry Circuit Inflow Pressure	0.968	0.320	-1.056	0.038	0.068	62
4	P1.1 Slurry Pump Suction Pressure	0.952	0.239	-0.859	0.049	0.052	62

Table 4 – continued from previous page

Ge	cological Regime	Variable	PICP	NMPIW	NLL	CRPS	Coverage Gap	Sample Size
	4	P1.1 Slurry Pump	1.000	0.473	-0.526	0.056	0.100	62
		Discharge Pressure						
	4	P2.1 Slurry Pump	0.919	0.241	-1.120	0.035	0.019	62
		Suction Pressure						
	4	P2.1 Slurry Pump	0.984	0.375	-0.973	0.040	0.084	62
	4	Discharge Pressure Slurry Inflow Rate	1.000	0.333	-0.603	0.054	0.100	62
	4	Slurry Inflow Rate	1.000		0.670		0.100	62
	•	Density	1.000	0.770	0.070	0.170	0.100	02
	4	Slurry Outflow	1.000	0.434	-0.178	0.087	0.100	62
		Rate						
	4	Slurry Outflow	0.968	0.364	-0.310	0.078	0.068	62
	-	Density	0.00=	0.505	0.424	0.050	0.00	
	5	Torque	0.987	0.525	-0.421		0.087	75 75
	5	Cutterhead Total Contact Force	0.987	0.527	-0.278	0.080	0.087	75
	5	Slurry Circuit	0.960	0.364	-1.173	0.035	0.060	75
	3	Inflow Pressure	0.700	0.504	-1.173	0.033	0.000	73
	5	P1.1 Slurry Pump	0.853	0.306	-0.436	0.080	0.047	75
		Suction Pressure						
	5	P1.1 Slurry Pump	0.987	0.196	-1.087	0.035	0.087	75
	_	Discharge Pressure						
	5	P2.1 Slurry Pump	0.987	0.375	-0.806	0.049	0.087	75
	5	Suction Pressure P2.1 Slurry Pump	0.960	0.418	-1.556	0.024	0.060	75
	3	Discharge Pressure	0.900	0.416	-1.550	0.024	0.000	13
	5	Slurry Inflow Rate	1.000	0.544	-0.666	0.056	0.100	75
	5	Slurry Inflow	1.000	1.009	0.935		0.100	75
		Density						
	5	Slurry Outflow	0.987	0.642	-0.487	0.062	0.087	75
	-	Rate	1 000	1.010	0.770	0.055	0.100	
	5	Slurry Outflow	1.000	1.042	-0.559	0.057	0.100	75
	6	Density Torque	0.988	0.948	0.505	0 167	0.088	86
	6	Cutterhead Total	0.988	0.610	0.035		0.088	86
	Ü	Contact Force	0.700	0.010	0.055	0.112	0.000	00
	6	Slurry Circuit	0.988	0.600	-0.694	0.052	0.088	86
		Inflow Pressure						
	6	P1.1 Slurry Pump	0.988	0.732	0.134	0.118	0.088	86
	_	Suction Pressure					0.05	0.5
	6	P1.1 Slurry Pump	0.965	0.164	-1.592	0.023	0.065	86
	6	Discharge Pressure P2.1 Slurry Pump	0.988	0.554	-0.731	0.054	0.088	86
	U	Suction Pressure	0.900	0.554	-0.731	0.034	0.000	80
	6	P2.1 Slurry Pump	0.977	0.453	-1.228	0.033	0.077	86
	-	Discharge Pressure			0		2.2	
	6	Slurry Inflow Rate	0.988	0.251	-0.881	0.045	0.088	86
	6	Slurry Inflow	0.953	0.543	0.311	0.148	0.053	86
	_	Density						
	6	Slurry Outflow	0.965	0.269	-0.658	0.055	0.065	86
		Rate						

Table 4 – continued from previous page

Geological Regime	Variable	PICP	NMPIW	NLL	CRPS	Coverage Gap	Sample Size
6	Slurry Outflow Density	0.977	0.443	-0.943	0.046	0.077	86
7	Torque	0.988	0.741	-0.322	0.075	0.088	80
7	Cutterhead Total Contact Force	0.963	0.408	-0.511	0.065	0.062	80
7	Slurry Circuit Inflow Pressure	0.938	0.164	-1.137	0.037	0.037	80
7	P1.1 Slurry Pump Suction Pressure	0.975	0.522	-0.414	0.069	0.075	80
7	P1.1 Slurry Pump Discharge Pressure	0.950	0.201	-1.649	0.020	0.050	80
7	P2.1 Slurry Pump Suction Pressure	0.963	0.432	-0.407	0.068	0.062	80
7	P2.1 Slurry Pump Discharge Pressure	0.988	0.504	-0.846	0.044	0.088	80
7	Slurry Inflow Rate	0.925	0.300	-0.626	0.064	0.025	80
7	Slurry Outflow Rate	0.950	0.337	-0.677	0.056	0.050	80
7	Slurry Outflow Density	0.950	0.355	-1.029	0.042	0.050	80
8	Torque	0.991	0.890	-0.093	0.095	0.091	108
8	Cutterhead Total Contact Force	0.972	0.611	-0.235	0.090	0.072	108
8	P1.1 Slurry Pump Suction Pressure	0.991	0.681	-0.279	0.080	0.091	108
8	P1.1 Slurry Pump Discharge Pressure	0.935	0.220	-1.648	0.022	0.035	108
8	P2.1 Slurry Pump Suction Pressure	0.991	0.707	-0.067	0.100	0.091	108
8	P2.1 Slurry Pump Discharge Pressure	0.972	0.390	-1.570	0.023	0.072	108
8	Slurry Inflow Rate	0.981	0.462	-0.628		0.081	108
8	Slurry Inflow Density	0.963	0.508	0.286	0.147	0.063	108
8	Slurry Outflow Rate	0.972	0.362	-0.669	0.059	0.072	108
8	Slurry Outflow Density	0.972	0.490	-1.537	0.024	0.072	108
9	Torque	0.952	0.452	-0.953	0.046	0.052	42
9	Slurry Circuit Inflow Pressure	0.929	0.449	-0.134	0.089	0.029	42
9	P1.1 Slurry Pump Discharge Pressure	1.000	0.426	-1.341	0.029	0.100	42
9	P2.1 Slurry Pump Suction Pressure	0.952	0.461	0.017	0.099	0.052	42
9	Slurry Inflow Rate	0.952	0.477	-1.119	0.038	0.052	42
9	Slurry Outflow Rate	0.905	0.342	-1.354	0.030	0.005	42
10	Torque	0.959		-0.250		0.059	123
10	Cutterhead Total Contact Force	0.943	0.520	-0.250	0.087	0.043	123

Geological Regime	Variable	PICP	NMPIW	NLL	CRPS	Coverage Gap	Sample Size
10	Slurry Circuit Inflow Pressure	0.976	0.612	-0.506	0.066	0.076	123
10	P1.1 Slurry Pump Suction Pressure	0.976	0.467	-0.221	0.087	0.076	123
10	P1.1 Slurry Pump Discharge Pressure	0.976	0.234	-1.078	0.035	0.076	123
10	P2.1 Slurry Pump Suction Pressure	0.967	0.463	-0.654	0.059	0.067	123
10	P2.1 Slurry Pump Discharge Pressure	0.967	0.234	-1.357	0.028	0.067	123
10	Slurry Inflow Rate	0.951	0.327	-0.860	0.045	0.051	123
10	Slurry Inflow Density	0.976	0.724	0.467	0.169	0.076	123
10	Slurry Outflow Rate	0.967	0.360	-0.605	0.057	0.067	123
10	Slurry Outflow Density	0.984	0.459	-0.773	0.047	0.084	123

D Data Preprocessing, Feature Engineering, and Selection

Along the temporal axis, missing observations are recovered using cubic spline interpolation with limited extrapolation at the boundaries. Residual gaps are conservatively imputed with column-wise medians to mitigate distortion from outliers. Anomalous samples are identified both at the univariate level, via a modified Z-score based on the Median Absolute Deviation (MAD):

$$Z_{ij}^{(M)} = 0.6745 \, \frac{x_{ij} - \text{median}(x_j)}{\text{MAD}(x_j)},$$
 (16)

and at the multivariate level, using the Mahalanobis distance:

$$D_M(\mathbf{x}_i) = \sqrt{(\mathbf{x}_i - \boldsymbol{\mu})^{\top} \Sigma^{-1} (\mathbf{x}_i - \boldsymbol{\mu})}.$$
(17)

Only the top 5% of extreme samples are trimmed to balance noise suppression and information retention. Here, x_{ij} denotes the j-th feature of sample i, $\operatorname{median}(\cdot)$ and $\operatorname{MAD}(\cdot)$ denote the columnwise median and Median Absolute Deviation, respectively; τ is the anomaly threshold; μ and Σ are the sample mean vector and covariance matrix, respectively.

After missing-value recovery and anomaly removal, the goal of feature engineering is to embed operational parameter couplings, sample distributional characteristics, and geological priors into learnable representations with minimal information loss, while simultaneously controlling dimensionality and estimation variance. Specifically, the cleaned passive parameter vector $\mathbf{z} = (z_1, \dots, z_p)^{\top}$ is mapped to second-order interaction terms, retaining only pure cross-products:

$$\Phi_{\text{int}}(\mathbf{z}) = \{ z_i z_j \mid 1 \le i < j \le p \}. \tag{18}$$

At the row level, statistical descriptors are extracted across the p-dimensional passive measurements at each time slice. For the i-th sample $\{z_{i1}, \ldots, z_{ip}\}$, we define the row mean and standard deviation as

$$\bar{z}_i = \frac{1}{p} \sum_{j=1}^p z_{ij}, \qquad s_i = \sqrt{\frac{1}{p-1} \sum_{j=1}^p (z_{ij} - \bar{z}_i)^2}.$$
 (19)

and the skewness and excess kurtosis as:

$$\gamma_{1,i} = \frac{\frac{1}{p} \sum_{j=1}^{p} (z_{ij} - \bar{z}_i)^3}{\left(\frac{1}{p} \sum_{j=1}^{p} (z_{ij} - \bar{z}_i)^2\right)^{3/2}}, \qquad \gamma_{2,i} = \frac{\frac{1}{p} \sum_{j=1}^{p} (z_{ij} - \bar{z}_i)^4}{\left(\frac{1}{p} \sum_{j=1}^{p} (z_{ij} - \bar{z}_i)^2\right)^2} - 3.$$
 (20)

To incorporate geological priors, let the geological vector of the *i*-th sample be $\mathbf{g}_i = (g_{i1}, \dots, g_{im})$, and construct aggregated quantities:

$$\psi_i^{\text{(sum)}} = \sum_{k=1}^m g_{ik}, \qquad \psi_i^{\text{(prod)}} = \prod_{k=1}^m g_{ik}.$$
(21)

and robust ratios:

$$\psi_{i,1}^{(\text{ratio})} = \frac{g_{i1}}{g_{i2} + \epsilon}, \qquad \psi_{i,2}^{(\text{ratio})} = \frac{g_{i3}}{g_{i4} + \epsilon}.$$
(22)

As interaction and composite terms are introduced, feature dimensionality grows rapidly. To preserve key information while suppressing redundancy, we define the expanded input matrix $\mathbf{X} \in \mathbb{R}^{n \times d}$. Near-constant columns are removed by variance thresholding:

$$Var(X_{\cdot j}) = \frac{1}{n-1} \sum_{i=1}^{n} (X_{ij} - \bar{X}_{\cdot j})^{2}.$$
 (23)

Mutual information is then used to quantify nonlinear dependence between features and the target variable y:

$$I(x_j; y) = \iint p(x_j, y) \log \frac{p(x_j, y)}{p(x_j)p(y)} dx_j dy.$$
(24)

Finally, recursive feature elimination (RFE) with Extremely Randomized Trees is applied. Let S_t denote the retained feature set at iteration t; in each round, r features with the lowest marginal contribution are removed, with cross-validation score $Score(\cdot)$ guiding the update:

$$S_{t+1} = \arg \max_{\substack{S \subset S_t \\ |S| = |S_t| - r}} \text{Score}\left(\widehat{f}_{\text{ET}}(\mathbf{X}_{\mathcal{S}}, y)\right). \tag{25}$$

Iteration continues until the retained dimensionality drops to the preset limit s.